CHAPTER 4

NUMERICAL METHODOLOGY

History prevails that a major thrust has always been to fly faster and higher, but they will be made reality only when computational fluid dynamics will develop to a point where the complete three-dimensional flow field over the vehicle can be computed rapidly with accuracy and consistency. The ground test facilities do not exist for all the flight regimes covered by hypersonic flight and quite expensive if available. Simulation of higher Mach number and high temperature flows encountered during the trans-atmospheric vehicle are of great challenge. Hence the major thrust in designing in designing of these vehicles is computational fluid dynamics. Computational fluid dynamics is an associate of theoretical and experimental aerodynamics. During early periods 1960, only two approaches were used to solve the fluid dynamics problems viz. the theoretical and the experimental. However with the development of the high speed digital computers and accurate numerical algorithms for solving physical problems has revolutionized the way we practice fluid dynamics today. Since computational fluid dynamics provides the third approach there will always be a need for theory and experiment. As shown in Fig. 4.1, the understanding of fluid dynamics will rest upon the proper balance of all the three approaches.

The results obtain from computational fluid dynamics are directly related to the wind tunnel results obtained as both represents the sets of data for a given flow configuration at different Mach number and Reynolds number. The data obtained from wind tunnel are exact scenario of the real world data which can be easily understand and a physical phenomenon happening can be seen. Though the experimental simulations give the real world data, which is easy to understand, it requires a costly experimental set up and tweaking of the setup for different

configurations of the model. Besides this, a wide range of different sophisticated instruments like Pitot tube, temperature sensors, anemometers are required to observe different parameter. In contrast, the computational fluid dynamic approach does not require a physical set up, and can model most physical phenomenon and can gather a huge amount of data by just solving the equations once.

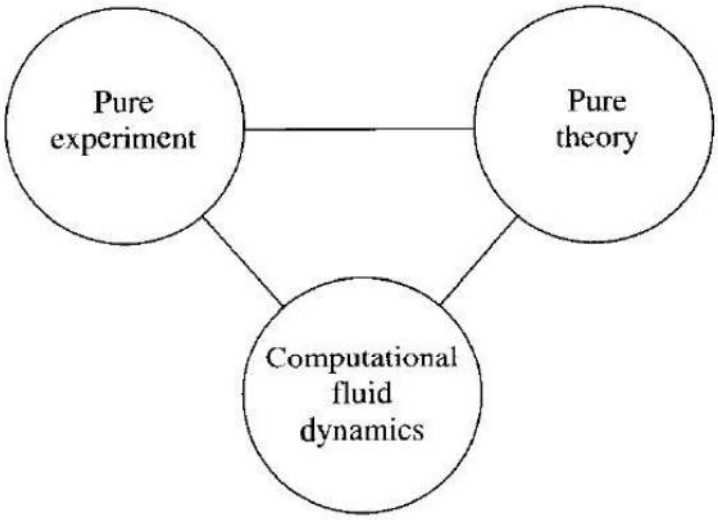

Fig. 4.1: Fluid Dynamics - Three Dimensions [66]

4.1. Computational Fluid Dynamics (CFD)

The analysis of any fluid flow problems are derived from the three basic fundamental principles viz., law of conservation of mass, law of conservation of momentum and law of conservation of energy. These fundamental physical principles can be expressed in terms of mathematical equations, which are in the form of either integral or partial differential equations. Computational fluid dynamics is the process of replacing the integrals or the partial derivatives equations in discretized algebraic forms, which in turns are solved to obtain numbers of flowfield values at discrete points in time and or space. The outcome is a collection of data, in contrast to a closed-form analytical integral or differential solution

The basic steps involved are:

a. Preprocessing

b. The geometry (physical bounds) of the problem is defined.

- The volume occupied by the fluid is divided into discrete cells (the mesh). The mesh may be uniform or non-uniform.
- The physical modeling is defined
- Boundary conditions are defined.

c. The simulation is started and the equations are solved iteratively as a steady-state or transient.

d. Finally a postprocessor is used for the analysis and visualization of the resulting solution.

In the present research the unsteady, compressible, turbulent, axisymmetric Reynolds-averaged Navier-Stokes (RANS) equations are solved in order to understand the basic fluid dynamics over the spiked blunt body at fixed atmospheric conditions using multidisk aerospikes. The governing equations can be expressed in different forms and notations depending upon the coordinate system and the model of the fluid [67] & [68].

4.2. The Governing Equations

The equations of fluid dynamics are based on the following universal laws of conservation viz. Conservation of Mass, Conservation of Momentum and Conservation of Energy. In addition to the equations developed from these universal laws, it is necessary to establish relationship between fluid properties in order to close the system of equations. The equation of state relates the thermodynamic variables pressure p, density ρ and temperature T so as to close the system of equations.

4.2.1. The Continuity Equation

The conservation of mass applied to a fluid passing through a control volume fixed in space yields the following equation of continuity:

$$\frac{\partial \rho}{\partial t} + \nabla \cdot (\rho V) = 0 \qquad 4.1$$

where ρ is the fluid density and V is the fluid velocity. The first term in the equation represent the rate of increase of density and the second term represents the rate of mass flux passing out of the control surface per unit volume.

For a Cartesian coordinate system, where u, v, w represent the x, y, z component of velocity vector, equation (4.1) becomes

$$\frac{\partial \rho}{\partial t} + \frac{\partial \rho}{\partial x}(\rho u) + \frac{\partial \rho}{\partial y}(\rho v) + \frac{\partial \rho}{\partial z}(\rho w) = 0 \qquad 4.2$$

The above equation is in the conservation form that is suitable for simulation of supersonic and hypersonic flows.

4.2.2. The Momentum Equation

The conservation of the linear momentum for any fixed control volume yields the following momentum equation.

$$\frac{\partial}{\partial t}(\rho V) + \nabla . \rho VV = \rho f + \nabla \cdot \pi_{ij} \qquad 4.3$$

In Equation (4.3), $\frac{\partial}{\partial t}(\rho V)$ is the time rate of change of momentum per unit volume ; $\nabla . \rho VV$ is the net outflow of momentum through the control surfaces; ρf represent the body per unit volume and $\nabla \cdot \pi_{ij}$ represent the surface force per unit volume where π_{ij} represent the stress tensor consist of normal and shearing stresses. The stress tensor π_{ij} in equation 4.3 can be expressed as given in Equation 4.4.

$$\pi_{ij} = -p\delta_{ij} + \mu\left(\frac{\partial u_i}{\partial x_j} + \frac{\partial u_j}{\partial x_i}\right) + \delta_{ij}\,\mu' \frac{\partial u_k}{\partial x_k} \qquad (i, j, k = 1,2,3) \qquad 4.4$$

where δ_{ij} is the Kronecker delta function; $u_1, u_2 \; and \; u_3$ represent the three component of the velocity vector $\boldsymbol{V}$; μ is the dynamic viscosity and μ' is the second coefficient of viscosity. The dynamic viscosity and the second coefficient of viscosity are related to each other via the bulk viscosity$K$, which is given by Equation 4.5.

$$K = \frac{2}{3}\mu + \mu' \tag{4.5}$$

However, K is almost negligibly small for Newtonian fluids i.e. with $K = 0$ the second coefficient of viscosity yields to Equation (4.6)

$$\mu' = -\frac{2}{3}\mu \tag{4.6}$$

The viscous stress tensor thus can be expressed as per Equation 4.7.

$$\pi_{ij} = -p\delta_{ij} + \mu\left[\left(\frac{\partial u_i}{\partial x_j} + \frac{\partial u_j}{\partial x_i}\right) - \frac{2}{3}\delta_{ij}\frac{\partial u_k}{\partial x_k}\right] \qquad (i, j, k = 1,2,3) \tag{4.7}$$

Thus, the final momentum equation can be given by Equation (4.8)

$$\rho\frac{DV}{Dt} = \rho f - \nabla \cdot p + \frac{\partial}{\partial x_j}\left[\mu\left(\frac{\partial u_i}{\partial x_j} + \frac{\partial u_j}{\partial x_j}\right) - \frac{2}{3}\delta_{ij}\mu\frac{\partial u_k}{\partial x_k}\right] \tag{4.8}$$

In terms of viscous stress tensor the above equation becomes

$$\rho\frac{DV}{Dt} = \rho f - \nabla \cdot p + \frac{\partial}{\partial x_j}[\tau_{ij}] \tag{4.9}$$

The above equation can be transformed into Cartesian coordinate system into three Navier Strokes equations in x, $y \; and \; z$ direction respectively.

The x-component of momentum equation:

$$\rho\frac{Du}{Dt} = \rho f_x - \frac{\partial p}{\partial x} + \frac{\partial}{\partial x}\left[\frac{2}{3}\mu\left(2\frac{\partial u}{\partial x} - \frac{\partial v}{\partial y} - \frac{\partial w}{\partial z}\right)\right] + \frac{\partial}{\partial y}\left[\mu\left(\frac{\partial u}{\partial y} + \frac{\partial v}{\partial x}\right)\right] + \frac{\partial}{\partial z}\left[\mu\left(\frac{\partial w}{\partial x} + \frac{\partial u}{\partial z}\right)\right] \quad 4.10a$$

The y-component of momentum equation:

$$\rho\frac{Dv}{Dt} = \rho f_y - \frac{\partial p}{\partial y} + \frac{\partial}{\partial x}\left[\left(\frac{\partial v}{\partial x} + \frac{\partial u}{\partial y}\right)\right] + \frac{\partial}{\partial y}\left[\frac{2}{3}\mu\left(2\frac{\partial v}{\partial y} - \frac{\partial u}{\partial x} - \frac{\partial w}{\partial z}\right)\right] + \frac{\partial}{\partial z}\left[\mu\left(\frac{\partial v}{\partial z} + \frac{\partial w}{\partial y}\right)\right] \quad 4.10b$$

The z-component of momentum equation:

$$\rho\frac{Dw}{Dt} = \rho f_z - \frac{\partial p}{\partial z} + \frac{\partial}{\partial x}\left[\left(\frac{\partial w}{\partial x} + \frac{\partial u}{\partial z}\right)\right] + \frac{\partial}{\partial y}\left[\mu\left(\frac{\partial v}{\partial z} + \frac{\partial w}{\partial y}\right)\right] + \frac{\partial}{\partial z}\left[\frac{2}{3}\mu\left(2\frac{\partial w}{\partial z} - \frac{\partial u}{\partial x} - \frac{\partial v}{\partial y}\right)\right] \quad 4.10c$$

These equations can also be re-written in conservative form as given in Equations 4.11 a, b and c.

The Conservative form of x-component of momentum equation:

$$\frac{\partial \rho u}{\partial t} + \frac{\partial}{\partial x}(\rho u^2 + p - \tau_{xx}) + \frac{\partial}{\partial y}(\rho uv - \tau_{xx}) + \frac{\partial}{\partial z}(\rho uw - \tau_{xz}) = \rho f_x \quad 4.11a$$

The Conservative form of y-component of momentum equation:

$$\frac{\partial \rho v}{\partial t} + \frac{\partial}{\partial x}(\rho uv - \tau_{xy}) + \frac{\partial}{\partial y}(\rho v^2 + p - \tau_{yy}) + \frac{\partial}{\partial z}(\rho uw - \tau_{yz}) = \rho f_y \quad 4.11b$$

The Conservative form of z-component of momentum equation:

$$\frac{\partial \rho w}{\partial t}+\frac{\partial}{\partial x}(\rho uw-\tau_{xz})+\frac{\partial}{\partial y}(\rho uw-\tau_{yz})+\frac{\partial}{\partial z}(\rho w^2+p-\tau_{zz})=\rho f_z \quad 4.11c$$

The elements of the viscous tensor stress τ_{ij} in above equations are given by Equations 4.12 (a) – (f)

$$\tau_{xx}=\frac{2}{3}\mu\left(2\frac{\partial u}{\partial x}-\frac{\partial v}{\partial y}-\frac{\partial w}{\partial z}\right) \quad 4.12a$$

$$\tau_{yy}=\frac{2}{3}\mu\left(2\frac{\partial v}{\partial y}-\frac{\partial u}{\partial x}-\frac{\partial w}{\partial z}\right) \quad 4.12b$$

$$\tau_{zz}=\frac{2}{3}\mu\left(2\frac{\partial w}{\partial z}-\frac{\partial u}{\partial x}-\frac{\partial v}{\partial y}\right) \quad 4.12c$$

$$\tau_{xy}=\quad \tau_{yx}=\mu\left(\frac{\partial u}{\partial y}+\frac{\partial v}{\partial x}\right) \quad 4.12d$$

$$\tau_{xz}=\quad \tau_{zx}=\mu\left(\frac{\partial w}{\partial x}+\frac{\partial u}{\partial z}\right) \quad 4.12e$$

$$\tau_{yz}=\quad \tau_{zy}=\mu\left(\frac{\partial v}{\partial z}+\frac{\partial w}{\partial y}\right) \quad 4.12f$$

4.2.3. The Energy Equation

The first law of thermodynamics viz. conservation of energy states that the rate of change of energy equals the sum of rate of heat addition and work done on fluid particle. When this is applied to the fluid passing through an infinitesimal volume

fixed in space, the energy equation for a viscous hypersonic flow can be obtained as given in Equation 4.13,

$$\frac{\partial E_t}{\partial t} + \nabla \cdot E_t V = \frac{\partial Q}{\partial t} - \nabla \cdot q + \rho f \cdot V + \nabla \cdot (\pi_{ij} \cdot V) \qquad 4.13$$

where E_t is the total energy per unit volume of the fluid and is given by Equation 4.13 *a.*

$$E_t = \rho \left(e + \frac{V^2}{2} + potential\ \ energ + \cdots\cdots\cdots \right) \qquad 4.13a$$

where *e* is the internal energy per unit mass. In the Equation (4.13), the first term on the left side i.e. $\frac{\partial E_t}{\partial t}$, represents the time rate of change of total energy in the control volume, while the second term on left hand side ($\nabla \cdot E_t \boldsymbol{V}$) reflects the total energy per unit volume lost by convection passing through control surfaces. The first term on the right side of Equation 4.13, $\frac{\partial Q}{\partial t}$ represents the rate of heat produced per unit volume and the second term $\nabla \cdot \boldsymbol{q}$ represents the heat lost by conduction per unit volume. The heat transfer $\boldsymbol{q}$ by conduction is given by the Fourier's law and is expressed as

$$\boldsymbol{q} = -k\, \nabla T \qquad 4.14$$

where *k* is the coefficient of thermal conductivity and *T* is the temperature. The third and fourth term on the right hand side of the equation represent the work done on the control volume by the body forces and the work done on the control volume by the surface forces. Thus Equation (4.13) states that an increase of energy in the system equals to the sum of work done on the system and the heat addition, which is the first law of thermodynamics.

The above equation can be transformed into Cartesian coordinate system as follows,

$$\frac{\partial E_t}{\partial t} - \frac{\partial Q}{\partial t} - \rho\left(f_x u + f_y v + f_z w\right) + \frac{\partial}{\partial x}\left(E_t u + \rho u - u\tau_{xx} - v\tau_{xy} - w\tau_{xz} + q_x\right) + \frac{\partial}{\partial y}\left(E_t v + \rho v - u\tau_{xy} - v\tau_{yy} - w\tau_{yz} + q_y\right) + \frac{\partial}{\partial z}\left(E_t w + \rho w - u\tau_{xz} - v\tau_{yz} - w\tau_{zz} + q_z\right) = 0 \qquad 4.15$$

where,

$$q_x = -K\,\frac{\partial T}{\partial x} \qquad 4.16a$$

$$q_y = -K\,\frac{\partial T}{\partial y} \qquad 4.16b$$

$$q_Z = -K\,\frac{\partial T}{\partial z} \qquad 4.16c$$

4.2.4. The Equation of State

The compressible viscous flow is represented by the Navier-Stokes equations that consist of continuity equation, three momentum equations and energy equation. The system contains five equations of six unknown flowfield variables (ρ, p, e, u, v, w). In aerodynamics, the assumption that air is a perfect gas can be applied i.e. it assumes that the intermolecular forces are negligible. For a perfect gas, the equation of state is given by Equation (4.17)

$$p = \rho RT \qquad 4.17$$

where R is the gas constant . This provides a sixth equation, and also introduces a seventh unknown namely T. The seventh equation that closes the entire system is the thermodynamic relation between state variables. Therefore additional

equations are required in order to establishes the relation between thermodynamic property and transport property viz. viscosity (μ) and thermal conductivity (K).
For a calorically perfect gas, the internal energy is related to temperature by the equation

$$e = C_v T \tag{4.18}$$

where C_v is the specific heat at constant volume. The coefficient of thermal conductivity (K) and viscosity (μ) are related to the thermodynamic variable under kinetic theory. According to Sutherland's formula thermal conductivity and viscosity are given by Equation (4.19 a) and (4.19b)

$$\mu = C_1 \frac{T^{3/2}}{T + C_2} \tag{4.19a}$$

$$K = C_3 \frac{T^{3/2}}{T + C_4} \tag{4.19b}$$

Where C_1 to C_4 are constant for a given gas. For air at moderate temperatures the values of constants are:

$$C_1 = 1.458X10^{-6}\ Kg/(m\,s\,\sqrt{K}), \qquad C_2 = 110\ K$$

$$C_3 = 2.495X10^{-3}\ (Kg\,m)/(s^3 K^{\frac{3}{2}}), \qquad C_2 = 194\ K$$

The coefficient of thermal conductivity and viscosity are related by a non-dimensional parameter known as Prandtl number. The Prandtl number (Pr) is defined as the ratio of frictional dissipation to the thermal conduction and is expressed as per Equation (4.20)

$$\mathrm{Pr} = \frac{C_p \mu}{k} \tag{4.20}$$

The Prandtl number is often used to determine the coefficient of thermal conductivity K once μ is known, since the ration $C_p / \Pr$ is approximately constant for most gases. Therefore thermal conductivity k can be analyzed as per Equation (4.21)

$$k = \frac{C_p}{Pr}\,\mu \tag{4.21}$$

4.3. Governing Equations in Vector Form

The compressible Navier-Stokes equations in Cartesian coordinates are often written in a compact vector form as given by Equations 4.22. This form is particularly suited for writing codes and applying similar numerical algorithm to all equations in the set.

$$\frac{\partial U}{\partial t} + \frac{\partial E}{\partial x} + \frac{\partial F}{\partial y} + \frac{\partial G}{\partial z} = 0 \tag{4.22}$$

where U, E, F and G are vectors given by

$$U = \begin{bmatrix} \rho \\ \rho u \\ \rho v \\ \rho w \\ E_t \end{bmatrix} \tag{4.22a}$$

$$E = \begin{bmatrix} \rho u \\ \rho u^2 + p - \tau_{xx} \\ \rho uv - \tau_{xy} \\ \rho uw - \tau_{xz} \\ (E_t + p)u - u\tau_{xx} - v\tau_{xy} - w\tau_{xz} + q_x \end{bmatrix} \tag{4.22b}$$

$$F = \begin{bmatrix} \rho v \\ \rho uv - \tau_{xx} \\ \rho v^2 + p - \tau_{yy} \\ \rho uw - \tau_{yz} \\ (E_t + p)v - u\tau_{xy} - v\tau_{yy} - w\tau_{yz} + q_y \end{bmatrix} \qquad 4.22c$$

$$G = \begin{bmatrix} \rho w \\ \rho uv - \tau_{xz} \\ \rho uw - \tau_{yz} \\ \rho w^2 + p - \tau_{zz} \\ (E_t + p)w - u\tau_{xz} - v\tau_{yz} - w\tau_{zz} + q_z \end{bmatrix} \qquad 4.22d$$

The first term in the vector Equation (4.22) refers to continuity equation as given by Equation (4.2), Similarly the second, third and fourth row in the vector equation corresponds to momentum Equation (4.11a, 4.11b and 4.11c), whereas the fifth row refers to energy Equation (4.15). It is easier to write the Navier-Stokes equation in this form as it is easy to write the desired numerical algorithm.

4.4. The Averaged Equations for Turbulent Flow

As per Hinze [70] "turbulent fluid motion is an irregular condition of flow in which the various quantities show a random variation with time and space coordinates so that statistically distinct average values can be discerned."

The unsteady Navier-Stokes equations are considered to govern turbulent flows in the continuum regime. Turbulent flow can be solved by the direct numerical simulation (DNS), which requires that all the relevant turbulence length scales be resolved from the smallest eddies to scales of the order of the physical dimensions of the problem. The computation need to be three-dimensional even if the time-

mean aspect of the flow are two-dimensional, and also the time step must be small enough that the small- scale motion can be resolved in a time accurate manner even if the flow is steady in a time-mean sense. Such requirement places a large demand on the computer resources, to the extent that only relatively simple flows at low Reynolds number can be computed directly with present day machines.

Another approach is the large-eddy simulation (LES) in which the large-scale structures of a turbulent flow is computed directly and only the effects of the smallest and more nearly isotropic eddies are modelled. This is accomplished by "filtering" the Navier -Stokes equation to obtain a set of equation that governs the "resolved" flow. This filtering , to be define below, is a type of space averaging of the flow variables over regions approximately equal to the size of the computational control volume cells. The computational efforts required for LES is less than that of DNS.

The main thrust of present day research in computational fluid mechanics and heat transfer in turbulent flows is through the time- averaged Navier stokes equations. These equations are also referred to the Reynolds equations of motion or Reynolds averaged Navier-Stokes (RANS) equations. Time averaging of the equations of motion gives rise to new terms, which can be interpreted as "apparent" stress gradient and heat flux quantity associated with the turbulent motion. These new quantitates must be related to the mean flow variables through turbulence models. Thus this approach on the turbulent flow problem through solving the Reynolds equations of motion does not follow entirely from first principles, since additional assumptions must be made to "close" the system of equations.

The Reynolds equations are derived by decomposing the dependent variables in the conservation equations into time-mean and fluctuating components and then time averaging the entire equation. Two type of averaging are presently used, the

classical Reynolds averaging and the mass weighted averaging of which Reynolds averaging is primarily used.

4.4.1. Reynolds Averaged Navier-Stokes Equation

The time averaging quantity $\overline{f}$ can be defined as per Equation (4.23)

$$\bar{f} \equiv \frac{1}{\Delta t}\int_{t_o}^{t_o+\Delta t} f dt \qquad 4.23$$

The randomly changing flow variables can be replaced by time averages and fluctuations in flow filed $(u, \bar{u}\ and\ u')$ as shown in Fig. 4.2. Therefore for a Cartesian coordinate system, we can now write the following fluid properties as per Equation (4.24)

$$u = \bar{u} + u' \qquad v = \bar{v} + v' \quad w = \overline{w} + w' \quad \rho = \bar{\rho} + \rho' \qquad 4.24(a)$$

$$p = \bar{p} + p' \qquad h = \overline{h} + h' \quad T = \overline{T} + T' \quad H = \overline{H} + H' \qquad 4.24(b)$$

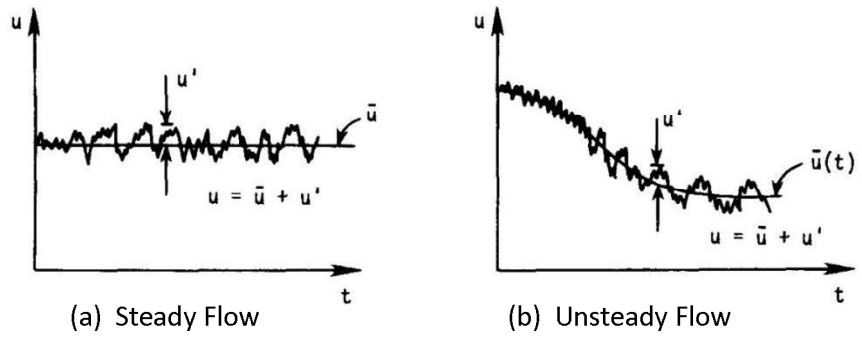

Fig. 4.2: Relation between $(u, \bar{u}\ and\ u')$ [69]

By definition the time average of the fluctuating quantity is zero:

$$\overline{f'} \equiv \frac{1}{\Delta t}\int_{t_o}^{t_o+\Delta t} f' dt \quad \equiv 0 \qquad 4.25$$

The mass averaged variables for the compressible flow is defined as per Equation 4.26.

$$\bar{f} = \overline{\rho f} \Big/ \bar{\rho} \qquad 4.26$$

The flow filed variables are mass- averages and thus given by Equations 4.27.

$$\bar{u} = \frac{\overline{\rho u}}{\bar{\rho}} \quad \bar{v} = \frac{\overline{\rho v}}{\bar{\rho}} \quad \bar{w} = \frac{\overline{\rho w}}{\bar{\rho}} \quad \bar{h} = \frac{\overline{\rho h}}{\bar{\rho}} \quad \bar{T} = \frac{\overline{\rho T}}{\bar{\rho}} \quad \bar{H} = \frac{\overline{\rho H}}{\bar{\rho}} \qquad 4.27$$

Substituting these into the conservation equations, the new fluctuating quantities are defines as

$$u = \bar{u} + u'', \qquad v = \bar{v} + v, \quad w = \bar{w} + w'', \; h = \bar{h} + h'',$$

$$T = \bar{T} + T'' \qquad and \qquad H = \bar{H} + H'' \qquad 4.28$$

The time average of a double primed fluctuation multiplied by the density is equal to zero as shown in Equation (3.29)

$$\overline{\rho f''} \equiv 0 \qquad 4.29$$

4.4.2. Reynolds Continuity Equation

The Reynolds form of the continuity equation in time averaged variables can be expressed as per Equation 4.30.

$$\frac{\partial \bar{\rho}}{\partial t} + \frac{\partial}{x_j}(\bar{\rho}\,\bar{u} + \overline{\rho' u'}) = 0 \qquad 4.30$$

Further substituting the mass-weighted averaged variables and the double primed functions, as expressed in Equation 4.28, into Equation 4.2 the Equation obtained in time averaging yields to Equation 4.31.

$$\frac{\partial}{\partial x_j}\left(\overline{\bar{\rho}u_j''}\right)+\frac{\partial}{\partial x_j}\left(\overline{\rho' u_j''}\right)=\frac{\partial}{\partial x_j}\overline{\rho u_j''} \tag{4.31}$$

This equation is equal to zero as per Equation 4.29 and therefore the continuity equation in mass-weighted variables can be written as Equation 4.32.

$$\frac{\partial \bar{\rho}}{\partial t}+\frac{\partial}{x_j}\left(\bar{\rho}\,\bar{u}_j\right)=0 \tag{4.32}$$

4.4.3. Reynolds Momentum Equation

The momentum equations given in Equation 4.11 can be converted to time averaged Reynolds momentum equations by replacing the dependent variable using Equation 4.24. The time averaged x- component of the momentum equation after neglecting the body forces can be written as Equation 4.33.

$$\begin{aligned}\frac{\partial}{\partial t}(\bar{\rho}\bar{u}+\overline{\rho' u'})+\frac{\partial}{\partial x}(\bar{\rho}\bar{u}\bar{u}+\bar{u}\overline{\rho' u'})+\frac{\partial}{\partial y}(\bar{\rho}\bar{u}\bar{v}+\bar{u}\overline{\rho' v'})+\frac{\partial}{\partial z}(\bar{\rho}\bar{u}\bar{w}+\bar{u}\overline{\rho' w'})\\ =-\frac{\partial \bar{p}}{\partial x}+\frac{\partial}{\partial x}\left[\mu\left(\frac{\partial \bar{u}}{\partial x}-\frac{2}{3}\frac{\partial \bar{u}_k}{x_k}\right)-\bar{u}\,\overline{\rho' u'}-\bar{\rho}\,\overline{u' u'}-\overline{\rho' u' u'}\right]\\ +\frac{\partial}{\partial y}\left[\mu\left(\frac{\partial \bar{u}}{\partial y}+\frac{\partial \bar{v}}{\partial x}\right)-\bar{v}\,\overline{\rho' u'}-\bar{\rho}\,\overline{u' v'}-\overline{\rho' u' v'}\right]\\ +\frac{\partial}{\partial z}\left[\mu\left(\frac{\partial \bar{u}}{\partial z}+\frac{\partial \bar{w}}{\partial x}\right)-\bar{w}\,\overline{\rho' u'}-\bar{\rho}\,\overline{u' w'}-\overline{\rho' u' w'}\right]\end{aligned} \tag{4.33}$$

The complete time averaged Reynolds momentum equation for all the three components can be written in tensor notation as Equation 4.34.

$$\begin{aligned}\frac{\partial}{\partial t}(\bar{\rho}\bar{u}_i+\overline{\rho' u'})+\frac{\partial}{\partial x_j}\left(\bar{\rho}\bar{u}_i\bar{u}_j+\bar{u}_i\overline{\rho' u_j'}\right)\\ =-\frac{\partial \bar{p}}{\partial x_i}+\frac{\partial}{\partial x_j}\left(\bar{\tau}_{ij}-\bar{u}_j\overline{\rho' u_i'}-\bar{\rho}\overline{u_i' u_j'}\right)-\overline{\rho' u_i' u_j'}\end{aligned} \tag{4.34}$$

where,

$$\bar{\tau}_{ij} = \mu\left[\left(\frac{\partial \bar{u}_i}{\partial x_j} + \frac{\partial \bar{u}_j}{\partial x_i}\right) - \frac{2}{3}\delta_{ij}\frac{\partial \bar{u}_k}{\partial x_k}\right] \quad 4.35$$

The Reynolds x- component of momentum equation in mass-weighted variables using decomposition variables as per Equation 4.28 becomes Equation 4.36.

$$\begin{aligned}\frac{\partial}{\partial t}\left[(\bar{\rho}+\rho')\left(\tilde{u}+u''\right)\right] + \frac{\partial}{\partial x}\left[(\bar{\rho}+\rho')\left(\tilde{u}+u''\right)\left(\tilde{u}+u''\right) + (\bar{p}+p') - \tau_{xx}\right] \\ + \frac{\partial}{\partial y}\left[(\bar{\rho}+\rho')\left(\tilde{u}+u''\right)\left(\tilde{v}+v''\right) - \tau_{yx}\right] \\ + \frac{\partial}{\partial z}\left[(\bar{\rho}+\rho')\left(\tilde{u}+u''\right)\left(\tilde{w}+w''\right) - \tau_{zx}\right] = 0 \quad 4.36\end{aligned}$$

The complete Reynolds momentum equation in mass weighted variable for all the three components yields to Equation 4.37.

$$\frac{\partial}{\partial t}(\bar{\rho}\tilde{u}_i) + \frac{\partial}{\partial x_j}\left(\bar{\rho}\tilde{u}_i\tilde{u}_j\right) = -\frac{\partial \bar{p}}{\partial x_i} + \frac{\partial}{\partial x_j}\left(\bar{\tau}_{ij} - \overline{\rho u_i'' u_j''}\right) \quad 4.37$$

where

$$\bar{\tau}_{ij} = \mu\left[\left(\frac{\partial \bar{u}_i}{\partial x_j} + \frac{\partial \bar{u}_j}{\partial x_i}\right) - \frac{2}{3}\delta_{ij}\frac{\partial \bar{u}_k}{\partial x_k}\right] + \mu\left[\left(\frac{\partial \overline{u_i''}}{\partial x_j} + \frac{\partial \overline{u_j''}}{\partial x_i}\right) - \frac{2}{3}\delta_{ij}\frac{\partial \overline{u_k''}}{\partial x_k}\right] \quad 4.38$$

4.4.4. Reynolds Energy Equation

Considering that the total energy composed of only internal energy and kinetic energy and re-writing the Equation (4.13) by replacing E_t with $(\rho H - p)$, the equation in summation notation becomes

$$\frac{\partial}{\partial t}(\rho H) + \frac{\partial}{\partial x_j}\left(\rho u_j H + q_j - u_i\tau_{ij}\right) = \frac{\partial p}{\partial t} \quad 4.39$$

Utilizing the static temperature as the dependent variable in the energy equation and replacing it with the decomposition form as given in Equation 4.24, the

resulting equation obtained is in time averaged form as expressed in Equation (4.40)

$$\frac{\partial}{\partial t}\left(c_p\bar{\rho}\bar{T} + c_p\overline{\rho' T'}\right) + \frac{\partial}{\partial x_j}\left(\bar{\rho}c_p\bar{T}\bar{u}_j + c_p\bar{T}\,\overline{\rho' u_j'}\right)$$
$$= \frac{\partial \bar{p}}{\partial t} + \bar{u}_j\frac{\partial \bar{p}}{\partial x_j} + \overline{u_j'\frac{\partial p'}{\partial x_j}}$$
$$+ \frac{\partial}{\partial x_j}\left(k\frac{\partial \bar{T}}{\partial x_j} - \bar{\rho}\,c_p\overline{T' u_j'} - c_p\overline{\rho' T' u_j'} - \bar{u}_j c_p\overline{\rho' T'}\right) + \bar{\Phi} \qquad 4.40$$

where $\bar{\Phi} = \overline{\tau_{ij}\frac{\partial u_i}{\partial x_j}} = \bar{\tau}_{ij}\frac{\partial \bar{u}_i}{\partial x_j} + \overline{\tau_{ij}'\frac{\partial u_j'}{\partial x_j}}$ 4.41

The Reynolds energy equation in mass-weighted variables can be obtained by using the fluctuation quantities illustrated in Equation 4.28 and averaging over time. The mass-weighted energy equation can thus be written as Equation 4.42.

$$\frac{\partial}{\partial t}(\bar{\rho}\,\bar{H}) + \frac{\partial}{\partial x_j}\left(\bar{\rho}\bar{u}_j\tilde{H} + \overline{\rho\, u_j'' H''} - K\frac{\partial \bar{T}}{\partial x_j}\right) = \frac{\partial \bar{p}}{\partial t} + \frac{\partial}{\partial x_j}(\bar{u}_i\bar{\tau}_{ij} + \overline{u_i''\tau_{ij}}) \qquad 4.42$$

The τ_{ij} in above equation can be evaluated using Equation 4.38. The Reynolds energy equation in terms of mass-weighted variable using static temperature then can be given by Equation 4.43.

$$\frac{\partial}{\partial t}(\bar{\rho}\,c_p\tilde{T}) + \frac{\partial}{\partial x_j}(\bar{\rho}c_p\tilde{T}\tilde{u})$$
$$= \frac{\partial \bar{p}}{\partial t} + \tilde{u}_j\frac{\partial \bar{p}}{\partial x_j} + \overline{u_j''\frac{\partial p}{\partial x_j}} + \frac{\partial}{\partial x_j}\left(k\frac{\partial \tilde{T}}{\partial x_j} + k\frac{\partial \bar{T}''}{\partial x_j} - c_p\overline{\rho T'' u_j''}\right)$$
$$+ \Phi \qquad 4.43$$

where

$$\overline{\Phi} = \overline{\tau_{ij}\frac{\partial u_i}{\partial x_j}} = \bar{\tau}_{ij}\frac{\partial \bar{u}_i}{\partial x_j} + \overline{\tau'_{ij}\frac{\partial u''_j}{\partial x_j}} \qquad 4.44$$

4.4.5. Conclusion from the Reynolds Equation

In turbulent flows, categorizing the terms according to the acceleration of the mean motion and actual stresses becomes more of a challenge. Using regular averaging, the presence of the terms like $\overline{\rho' u'_i}$ results in the flux of momentum across mean flow streamlines. Further the use of mass-weighted averaging eliminates the $\overline{\rho' u'_i}$ terms and provides an expression for particle acceleration but complicate the separation of stresses into purely laminar and apparent turbulent categories. In time average, the fluctuating component of $\bar{\tau}_{ij}$vanishes. The momentum Equation 4.34 can be rearranged in substantial derivative as follows in Equation 4.45.

$$\bar{\rho}\frac{\mathrm{D}\tilde{u}_i}{\mathrm{D}t} = -\frac{\partial \bar{p}}{\partial x_i} + \frac{\partial(\bar{\tau}_{ij})_{lam}}{\partial x_j} + \frac{\partial(\bar{\tau}_{ij})_{tur}}{\partial x_j} \qquad 4.45$$

The first on the left hand side is the particle acceleration of mean motion, the first term on the right hand side is the mean pressure gradient, while the second term represents the laminar stress gradient for the mean flow, the last term expresses the apparent stress gradient due to transport of momentum by turbulent fluctuations and deformations attributed to fluctuations.

In Equation 4.45,

$$(\bar{\tau}_{ij})_{lam} = \mu\left[\left(\frac{\partial \bar{u}_i}{\partial x_j} + \frac{\partial \bar{u}_j}{\partial x_i}\right) - \frac{2}{3}\delta_{ij}\frac{\partial \bar{u}_k}{\partial x_k}\right] \qquad 4.45a$$

and

$$(\bar{\tau}_{ij})_{turb} = -\overline{\rho u''_i u''_j} + \mu\left[\left(\frac{\partial \overline{u''_i}}{\partial x_j} + \frac{\partial \overline{u''_j}}{\partial x_i}\right) - \frac{2}{3}\delta_{ij}\frac{\partial \overline{u''_k}}{\partial x_k}\right] \qquad 4.45b$$

Since the viscosity fluctuations have been neglected in analyzing Equation 4.45, the third term in the equation $(\bar{\tau}_{ij})_{tur}$ involves the molecular viscosity.

Similarly in the energy equation given by Equation 4.40 the molecular "laminar-like" heat flux term is expressed as

$$-(\nabla.q)_{lam} = \frac{\partial}{\partial x_j}\left(k\frac{\partial \bar{T}}{\partial x_j}\right) \qquad 4.46a$$

And the apparent Reynolds turbulent heat flux is expressed as per Equation 4.46 b.

$$(\nabla.q)_{turb} = \frac{\partial}{\partial x_j}\left(-\bar{\rho}\, c_p \overline{T'u_j'} - c_p\overline{\rho'T'u_j'} - \bar{u}_j c_p \overline{\rho'T'}\right) \qquad 4.46b$$

The Reynolds equations therefore cannot be solved in the above form as the new heat flux quantitates and turbulent apparent stresses can be viewed as new unknowns. Therefore we need additional equations that relate the apparent turbulent quantities and the time-mean flow variables to close the problem which can be done through turbulence modeling.

4.5. Turbulence Modeling

Turbulence plays an important role in defining the aerodynamic forces and heating for hypersonic vehicles. Due to the extremely high speed in hypersonic flows, the experimental tests have discrepancies with the similar freestream enthalpy levels typical of hypersonic flight. The authentication of turbulence models with wind tunnel data thus generally involves substantial extrapolation to flight data. For this reason, the difficulties in attaining validation data for turbulent, hypersonic flows, designers are forced to rely heavily on associated models for turbulence and computational fluid dynamics.

Turbulence modeling therefore plays an important role while performing Reynolds Averaged Navier-Stokes equations (RANS) simulations. Since turbulent flows are present in many hypersonic applications and the phenomenon such as shock wave boundary layer interaction and boundary layer separation depends strongly on the superior choice of turbulent model. As per Boussinesq assumption (1877), the apparent turbulent shearing stresses can be related to the rate of mean strain through an eddy viscosity. For a Reynolds stress the Boussinesq assumption gives,

$$-\overline{\rho u_i' u_j'} = 2\mu_T S_{ij} - \frac{2}{3}\delta_{ij}\left(\mu_T \frac{\partial u_k}{\partial x_k} + \rho\bar{k}\right) \qquad 4.47$$

where μ_T is the turbulent viscosity, $\bar{k}$ is the kinetic energy of turbulence

$$S_{ij} = \frac{1}{2}\left(\frac{\partial u_i}{\partial x_j} + \frac{\partial u_j}{\partial x_i}\right) \qquad 4.48$$

To close the Reynolds Averaged Navier Stokes equations, the Boussinesq assumption were applied that are normally referred to as category I or turbulent viscosity also referred to as first-order model. Experimental evidence reveals that turbulent viscosity hypothesis is valid in most of the flow conditions. Models without Boussinesq assumption are referred to as category II models and include terms those known as stress equation model. These stress equations are referred as second–order closure. The other classification of models is according to the supplementary partial differential equations, which are to be solved in order to supply the modeling parameters. These numbers range from 0 for the simplest algebraic model to 12 for the most complex of Reynolds stress models as illustrated by Donaldson and Rosenbaum(1968)[67].

The third category model is defined as those which are not entirely based on Reynolds equations, such as large eddy simulations (LES). So a set of modified conservation equations is solved instead of Reynolds equation. Since the present

research to investigate the aerodynamic characteristics of a hypersonic vehicle with a forward facing aerospike at high Reynolds number, flow is assumed to be turbulent and an appropriate model needs to be implemented. Number of investigation and research has been done to suggest the appropriate turbulent model which can best fit for hypersonic flow [71] [72]. The appropriate model should be cheap, robust and should require minimum commuter time and storage, without compromising the accuracy the solution. Two of the most popular and reliable turbulence models for hypersonic flows are the one Equation Spalart-Allmaras Model (eddy viscosity transport model) [73-74] and the two equation *k-ω* models viz. the Wilcox *k-ω* model and Menter Shear Stress Transport model *k-*ω (SST) [71]. These models have been validated extensively for hypersonic flight regime and can be found in literature [75-78].

The Spalart–Allmaras one equation model solves a transport equation for modified eddy viscosity near the wall. This is based on the assumption that the Reynold stress tensor ($-\overline{\rho u_i' u_j'}$) is related to the mean strain rate through an apparent turbulent viscosity called eddy viscosity ν_t through Equation 4.49 [73] [74].

$$-\overline{\rho u_i' u_j'} = \nu_t \left(\frac{\partial \overline{u_i}}{\partial y^j} + \frac{\partial \overline{u_j}}{\partial y^i} \right) \qquad 4.49$$

The accuracy and estimations with Spalart-Allmaras model are insensitive to the y^+spacing at the wall relative to the two-equation models, atleast for hypersonic flow [78]. The Spalart-Allmaras model has a good accuracy and shows robustness for attached flow. Despite the fact that it is stable for large values of y^+, the maximum for accurate solutions should be roughly $y^+ \leq 1$. The Wilcox 1988 k-ω model is normally better than the k-ε model for wall-bounded flows, particularly in the presence of adverse pressure gradient. It is recommended that the y^+ values at the wall be kept well below one. The problem with Wilcox *k-* ω model

[71] is the sensitivity of the results to the freestream ω levels. The Menter SST *k*-ω model is a blending of the *k*-ω model near the wall and a transformed *k*-ε model in shear layers and a freestream and yields good results for a wide range of flows [77]. In this the turbulent viscosity is redefined to account for the transport of the turbulent shear stress. With the above reasons, it is seen that for aerospace applications the Spalart-Allmaras a one-equation model is designed especially for aerospace and takes kinematic eddy i.e. a turbulent viscosity into account. An aerospace application involves wall-bounded flows and one equation model Spalart-Allmaras gives acceptable results for boundary layers subject to adverse pressure gradient. Therefore in the present research the Spalart-Allmaras one equation model is chosen to model the effect of turbulence.

4.5.1. The Spalart – Allmaras (SA) Model

The Spalart-Allmaras model is a good compromise between algebraic and two-equation turbulence models. In general the SA model directly solves the transport equation for eddy viscosity, and it has become quite popular because of its compatibility with wide range of flow problems and numerical techniques [73] & [74]. The transport variable in the SA model $\tilde{\nu}$, which is identical to the turbulent kinetic viscosity except near walls where viscous affect are dominates. The governing transport equation for turbulent kinematic viscosity $\tilde{\nu}$ is given by Equation 4.50.

$$\frac{\partial}{\partial t}(\rho\tilde{\nu}) + \frac{\partial}{\partial x_i}(\rho\tilde{\nu}u_i) = G_\nu + \frac{1}{\sigma_{\tilde{\nu}}}\left[\frac{\partial}{\partial x_j}\left\{(\mu + \rho\tilde{\nu})\frac{\partial\tilde{\nu}}{\partial x_j}\right\} + C_{b2}\rho\left(\frac{\partial\tilde{\nu}}{\partial x_j}\right)^2\right] - Y_\nu + S_{\tilde{\nu}} \qquad 4.50$$

In above equation, the term G_ν is represents the production of turbulent viscosity and Y_ν represents the destruction of turbulent viscosity which occur near the wall region due to viscous damping and wall blocking. The term ν is the molecular

kinematic viscosity and $\sigma_{\tilde{\nu}}$ and C_{b2} are constants. $S_{\tilde{\nu}}$ is a user-defined source term in Equation 4.50.

4.5.2. Turbulent Viscosity Modeling

The computation of turbulent kinematic viscosity $\tilde{\nu}$ leads to the calculation of the turbulent viscosity μ_t through Equation 4.51.

$$\mu_t = \rho \tilde{\nu} f_{\nu 1} \tag{4.51}$$

The viscosity damping function $f_{\nu 1}$ in Equation 4.51 is expressed as

$$f_{\nu 1} = \frac{\chi^3}{\chi^3 + C_{\nu 1}^3} \tag{4.52}$$

where,

$$\chi \equiv \frac{\tilde{\nu}}{\nu} \tag{4.53}$$

4.5.3. Turbulent Production Modeling

The production of turbulent viscosity term, G_ν in Equation 4.51 is expressed as

$$G_\nu = C_{b1}\, \rho\, \tilde{S}\, \tilde{\nu} \tag{4.54}$$

where

$$\tilde{S} \equiv S + \frac{\tilde{\nu}}{k^2 d^2} f_{\nu 2} \tag{4.55}$$

and

$$f_{\nu 2} = 1 - \frac{\chi}{1 + \chi\, f_{\nu 1}} \tag{4.56}$$

The term C_{b1} and k are constants, the distance from the wall is d , and S is the deformation tensor and is based on the magnitude of the vorticity and is expressed as Equation 4.57.

$$S \equiv \sqrt{2\,\Omega_{ij}\Omega_{ij}} \tag{4.57}$$

where the term Ω_{ij} represent the mean rate-of-rotation tensor and is defined by Equation 4.58.

$$\Omega_{ij} = \frac{1}{2}\left(\frac{\partial u_i}{\partial x_j} - \frac{\partial u_j}{\partial x_i}\right) \tag{4.58}$$

However, in the current simulations an alternative formulation of the SA model that takes both vorticity and the strain based productions of turbulence into account is considered as given by Equation 4.59 [79].

$$S \equiv |\Omega_{ij}| + C_{prod} \min\left(0,\ |S_{ij}| - |\Omega_{ij}|\right) \tag{4.59}$$

where

$$C_{prod} = 2.0\,, \quad |\Omega_{ij}| = \sqrt{2\,\Omega_{ij}\Omega_{ij}}\,, \quad |S_{ij}| \equiv \sqrt{2\,S_{ij}S_{ij}} \tag{4.60}$$

The mean strain rate S_{ij} is defined as

$$\mathrm{S}_{ij} = \frac{1}{2}\left(\frac{\partial u_j}{\partial x_i} - \frac{\partial u_i}{\partial x_j}\right) \tag{4.61}$$

This includes both strain tensors and rotations which reduces the production of eddy viscosity in regions where the measure of vorticity surpasses that of strain rate.

4.5.4. The Turbulent Destruction Modeling

The destruction term in the SA model is modeled as

$$Y_\nu = C_{w1}\,\rho\, f_w \left(\frac{\nu}{d}\right)^2 \qquad 4.62$$

where

$$f_w = g\left[\frac{1 + C_{w3}^6}{g^6 + C_{w3}^6}\right]^{1/6} \qquad 4.62a$$

with

$$g = r + C_{w2}(r^6 - r) \qquad 4.62b$$

and

$$r = \frac{\tilde{\nu}}{\tilde{S}k^2d^2} \qquad 4.62c$$

In above equations, C_{w1}, C_{w2}, and C_{w3} are constants and $\tilde{S}$ is given by Equation (4.61). This modification includes the effect of mean strain on $\boldsymbol{S}$.

4.5.5. Model Constants

The model constants that appear in Equations 4.52-4.62, viz. C_{b1}, C_{b2}, $\sigma_{\tilde{\nu}}$, $C_{\nu 1}$, C_{w1}, C_{w2}, C_{w3}, and, k have been given following values in this simulation, as given by Equation 4.63.

$$C_{b1} = 0.1355, \qquad C_{b2} = 0.622, \qquad C_{\nu 1} = 7.1, \qquad \sigma_{\tilde{\nu}} = \frac{2}{3}$$

$$C_{w1} = \frac{C_{b1}}{k^2} + \frac{(1 + C_{b2})}{\sigma_{\tilde{\nu}}}, \quad C_{w1} = 0.3, \quad C_{w3} = 2.0, \quad k = 0.4187 \qquad 4.63$$

4.6. Geometric Modeling and Grid Generation

Geometric modeling and grid generation play a vital role in the field of numerical simulation of fluid dynamic systems. The solution of any problems is defined at

nodes inside the cell and the accuracy of the computational techniques is governed by the numbers of cells in the grid. Both the accuracy of a solution and its cost in terms of hardware and calculation time depend on the fineness of the grid. Optimal meshes are often non-uniform, finer in areas where large variations occur from point to point and coarser in regions with relatively little change.

4.6.1. Geometric Modeling

In the present investigation all the geometries are constructed using commercially available software Gambit. Gambit is a geometry and mesh generating software from ANSYS. Gambit is single interface for geometry creation and meshing that brings together most of the computational pre-processor techniques in one environment. The base configuration selected for studying the effect of aerospikes is a popularly investigated hemisphere cylinder with a base diameter 40 *mm* [55]. The axisymmetric hemisphere cylinder has length of 1.25D where D is the base diameter, as shown in Fig. 4.3.The subsequent models have aerospikes of various lengths and design, protruding from the stagnation point of the hemisphere cylinder as shown in Figs. 4.4, 4.5 and 4.6. Three types of aerodisks, viz., hemispherical aerodisk, flat triangular aerodisk and flat aerodisk have been investigated. The diameter of the aerospike stem for configuration is fixed at 0.1D, where D is the diameter of the base body. The overall spike lengths *l* of 1.0D, 1.5D, 2.0D and 2.5D were investigated in the present research with the radii disk varied between 0.05D, 0.1D, 0.15D and 0.2D.

4.6.2. Geometric Parameter Variations

Three important parameters viz. the *l/D* ratio, the radii of the aerodisks and the internal position of the intermediate disks on the spike, are identified for their effects on the aerodynamic drag and heat fluxes. The *l/D* ratio is varied from 1 to 2.5 for all the aerodisks configurations. The *l/D* ratio is varied from 1 to 2.5 because of practical applicability of these lengths based on extensive literature review. Most of the paper available in published literature reports the effect of *l/D* ratios, but the effect of aerodisk size is not studied. It is obvious that size of

aerodisk significantly modifies the flow field ahead of the blunt body and hence affects the aerodynamic parameters. Keeping this in view the radii of the front aerodisk is varied from 0.05D to 0.2D, keeping other geometric parameters fixed. The radii of intermediate aerodisk are bigger in size from the upwind aerodisk by an amount of 0.05D (2*mm*). The current research elaborates the effectiveness of multidisk aerospikes, thus for a given *l/D* ratio and size of the front aerodisks, the intermediate location of the rearward aerodisk can have a significant effect on the flow field ahead of the blunt body. So the third parameter of interest investigated in this research is the intermediate positioning of the rearward aerodisk. For the two disk aerospikes of given *l/D* ratio, the intermediate disk is placed at either *0.25l, 0.5l* or 0.*75l* with *l* as the length aerospike. For the three disk aerospike, for a given positions of rear aerodisk, the intermediate disk is positioned at *0.25, 0.5* or 0.*75* of the distance between the front and the rear disks, the rear disk position also being varied as with the two disk case. All the parameters have been varied for three different shapes of aerodisk viz. hemispherical aerodisk, flat triangular aerodisk and flat aerodisk. Combining the variations of all the above set geometric parameters, the various geometric configurations that have been identified for numerical simulations are listed in the **Appendix A**.

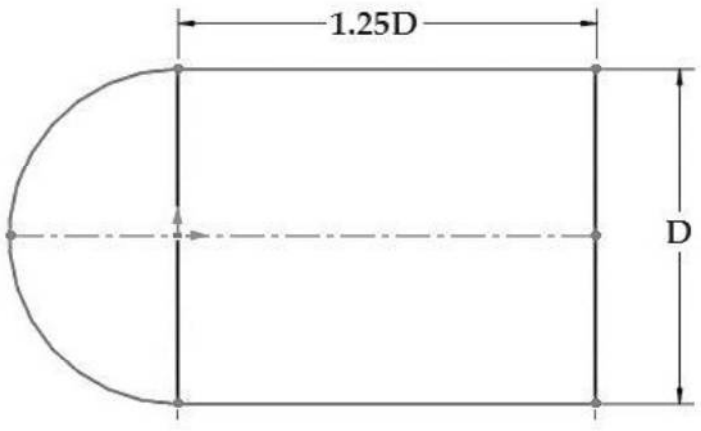

Fig. 4.3: Base geometry

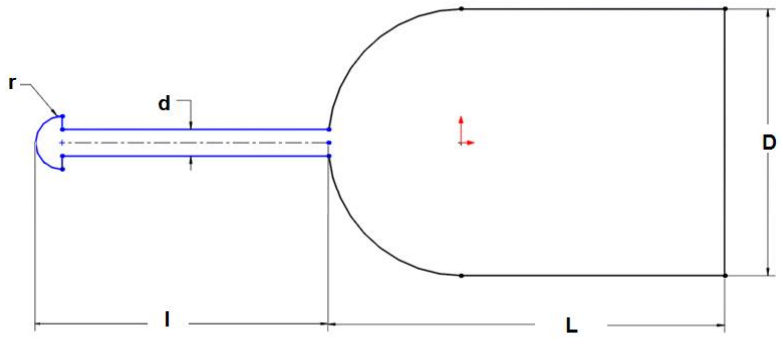

(a) Single Aerodisk

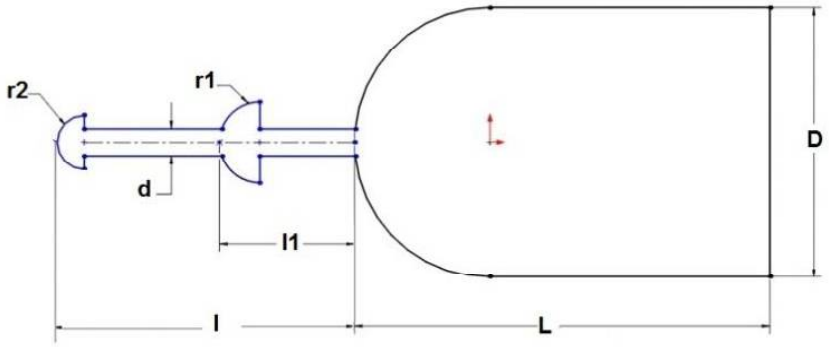

(b) Double Aerodisk

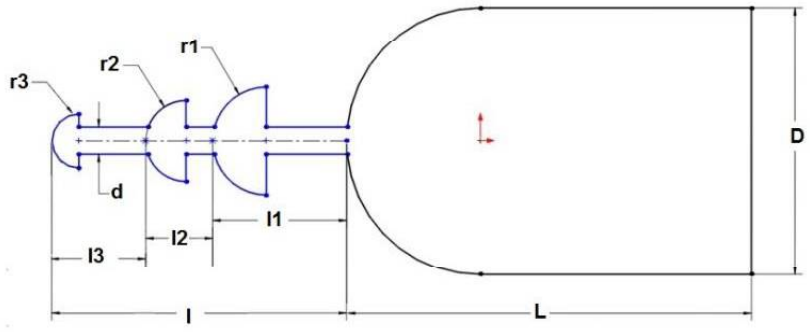

(c) Triple Aerodisk

Fig.4.4: Hemispherical Aerodisks

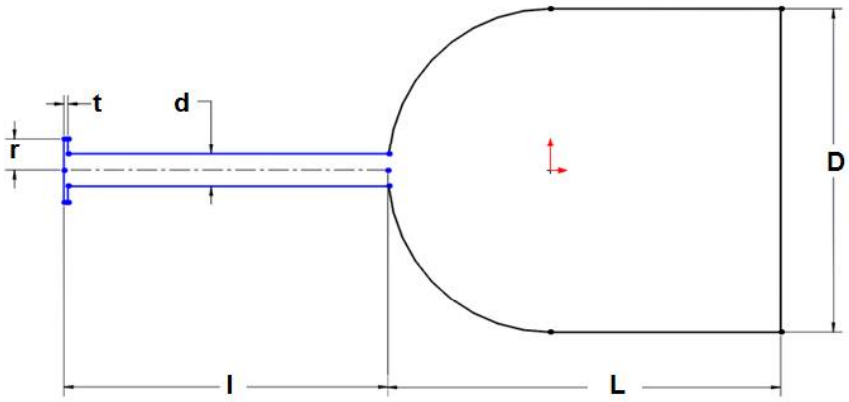

(a) Single Aerodisk

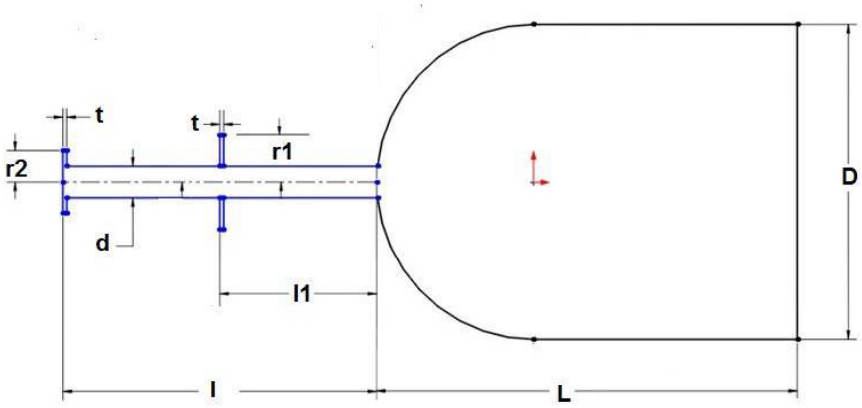

(b) Double Aerodisk

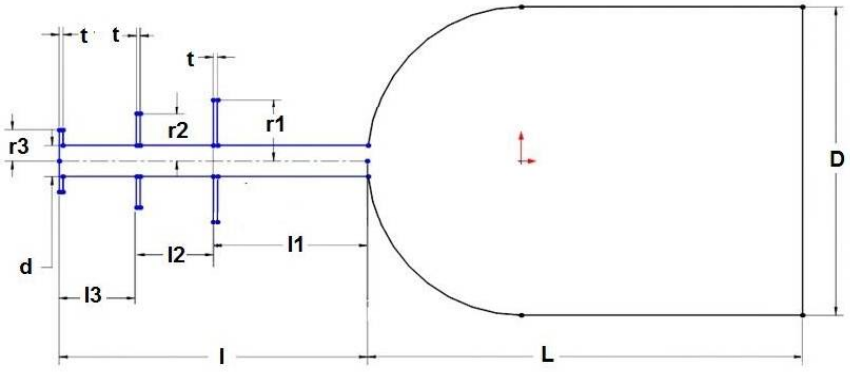

(c) Triple Aerodisk

Fig.4.5: Flat Aerodisk

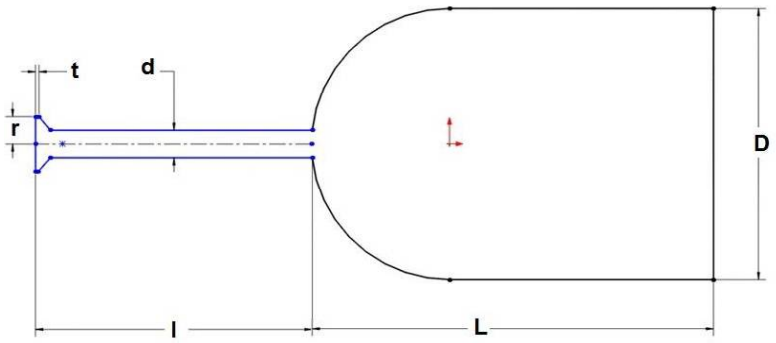

(a) Single Aerodisk.

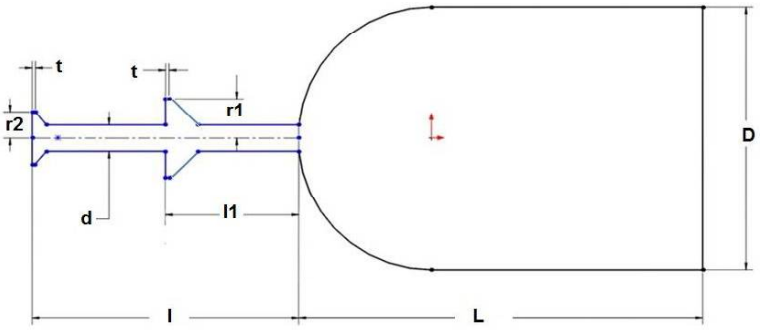

(b) Double disk.

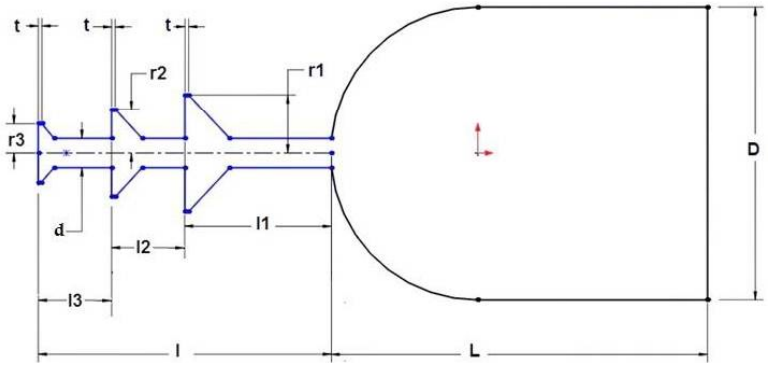

(c) Triple Aerodisk.

Fig.4.6: Flat Triangular Aerodisk

4.6.3. Grid Generation

To solve the partial differential equations the domain has to be discretized i.e. divided into a number of cells where the solution can be represented. Numerical solutions are often represented as a point value to find the fluid properties at a local grid points or as the average of the quantities over one cell as shown in Fig. 4.7.

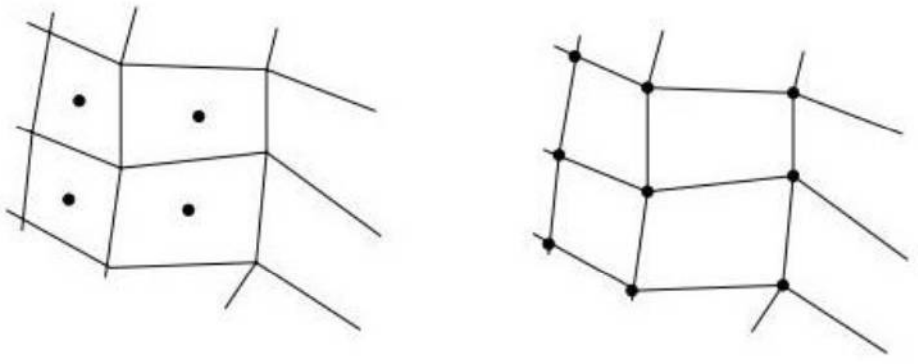

Fig. 4.7: Cell centers and grid points

The partial differential equations are integrated over the discretized domain using finite volume techniques to yield solutions at the grid points. Two different types of approaches are normally used to discretized a complex geometry viz. structured grid and unstructured grid as shown in Fig. 4.8. Structured grid generation methods rely on regular array of quadrilateral or hexahedral cells in two or three dimensions respectively; on the other hand the unstructured grid methods originally emerged as a viable alternative to the structure grid techniques for discretizing complex geometry. These methods make use of either collection simplicial elements or an element of mix type with irregular connectivity. This provides for greater flexibility for discretizing complex domain but lacks straightforward implementation of adaptive meshing techniques [80]. In the present research, a hybrid mesh is generated for the base body and for the

different aerospike varying *l/D* ratios, which has highly structured mesh in the boundary layers and an unstructured mesh at complex corners.

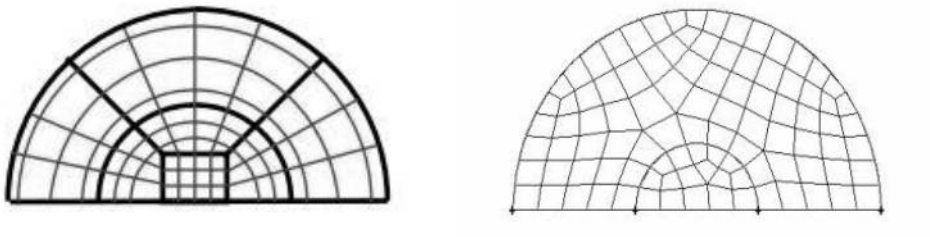

(a) Structured Grid (b) Unstructured Grid

Fig. 4.8: Types of grids

The initial mesh generated for the base body has a total cell of 50,000 quadrilaterals with the distance of the first cell from the body is 1e-06 m, such that the non-dimensional wall distance at the body is $y^+ \simeq 1$ for turbulent computation. A total of 20 rows structured grid was generated near the wall of the model stretched in the radial direction with a growth factor of 1.2, such that the grid near the wall is dense enough to resolve the viscous stresses. For all the mesh generated outside the prismatic boundary layer paving techniques has been used to generate the all quadrilateral meshes, which allows varying element size distribution on the boundary as well as the interior region. In this the mesh contour tends to follow geometric contours of the boundary. The paving techniques tend to place well-formed elements along the boundary with irregular nodes in the interior of the geometry [81]. A sizing function with start size of 0.1 *mm* has been applied which results in gradual increase in the size of quadrilateral as we travel away from the solid boundary. The smallest quadrilaterals adjacent to the prismatic boundary layer are of size 0.1 *mm* x 0.1 *mm* and largest quadrilaterals near the farfield are 2*mm* x 2*mm* in area. With the addition of the single aerodisk, double aerodisk and triple aerodisk of various geometries, protruding from the stagnation point of the nose of the base bodies, the cell count subsequent geometry varied from 60,000 to 90,000 in number. The initial meshes for the base configuration and configurations with hemispherical aerodisks are

shown in Fig. 4.9. These initial meshes were adapted a number of times during the course of solution in the regions of high gradients of pressures and temperature such that the final count of cells reached up to 200,000 in all cases as shown in Fig. 4.10. The refinement of meshes were stopped beyond 200,000 cells are the solutions were found to be grid independent with these numbers.

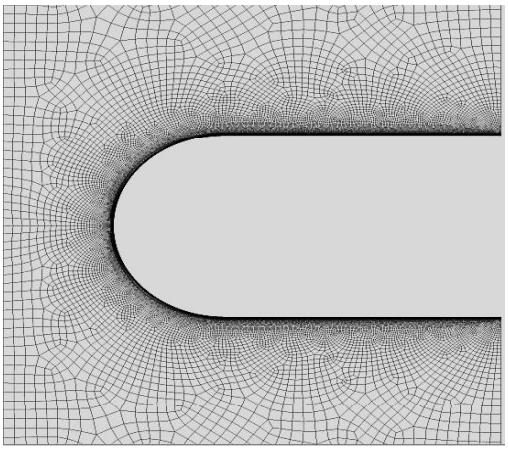

(a) Base body

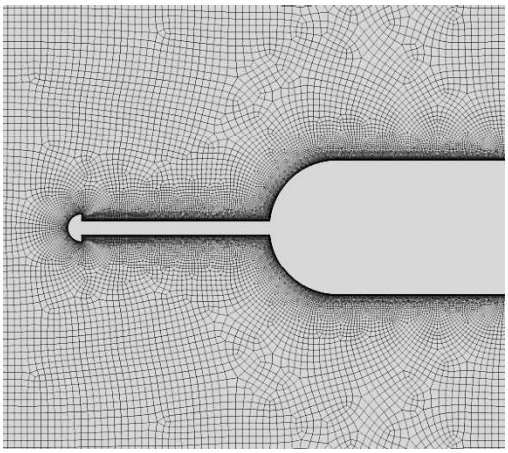

(b) Single disk spike

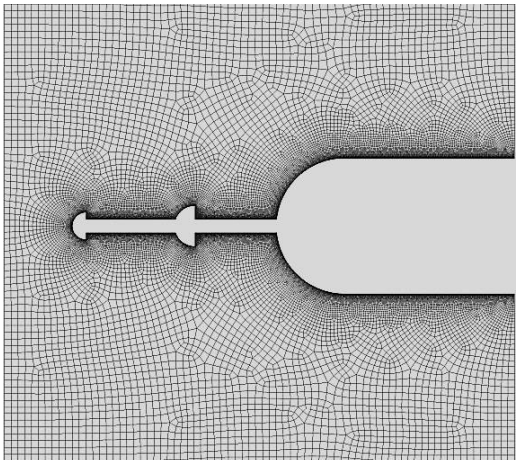

(c) Double disk aerospike

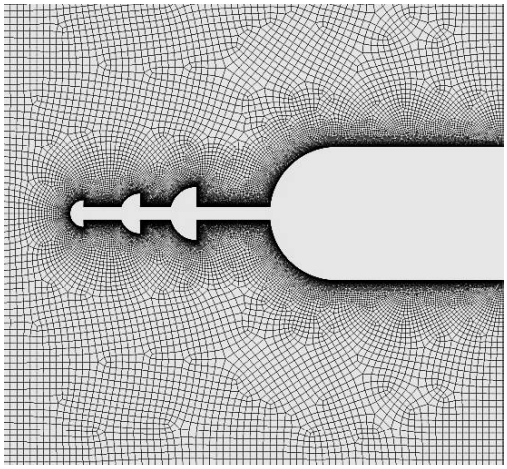

(d) Three disk aerospike.

Fig. 4.9: Initial Meshes around Hemispherical Aerodisks

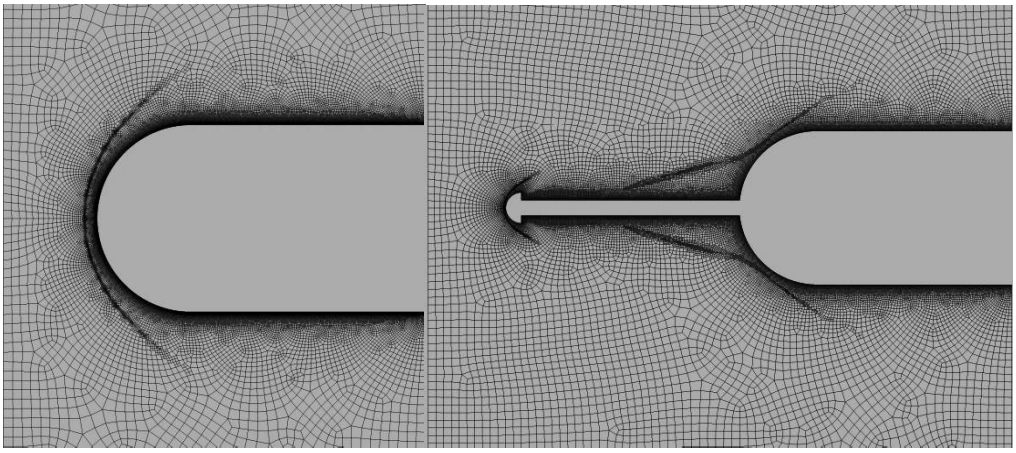

(a) Base body (b) Single disk Aerospike

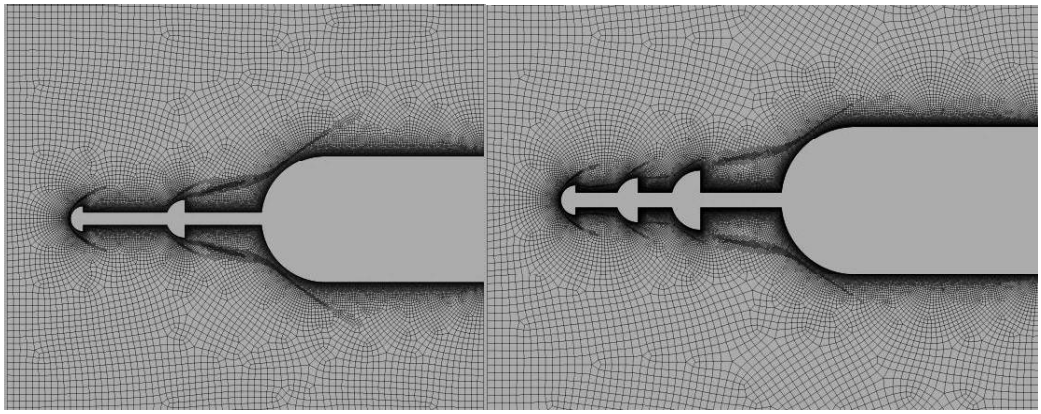

(c) Double disk Aerospike (d) Three disk Aerospike.

Fig. 4.10: Adapted Meshes around Hemispherical aerodisks

4.7. Solver Setting

The CFD software used in the investigation offers both the pressure and density based solvers. Since the present research deals with highly compressible flows at hypersonic speeds, a destiny-based solver is be used. In this, the density field is obtained from the continuity equation and the velocity field from the momentum equation in a coupled manner. The non-linear and coupled governing equations are solved iteratively using control volume based techniques till converged solutions are obtained.

The non-linear governing equations are linearized to obtain a system of equations for the dependent variables in every computational cell. The resultant linear coupled systems of governing equations are then solved to give an updated flow-filed solution using implicit formulation. In this the unknown value in each cell is computed using a relation that includes both current and unidentified values from adjacent cells. Each equation in the coupled form is linearized implicitly with respect to all dependent variables in the set. This results result in a system of N linear equations in each cells in the domain, where N is the number of coupled equations. This is referred as "block" system of equation. In general the coupled implicit approach solves all the variables $(\rho, u, v, \ w \ and \ T)$ in all cells at the same time.

4.7.1. Scalar Transport Equation and Discretization

Discretization is the process of transforming the continuous function and equations into discrete counterparts. The Fluent code uses a finite volume approach to transform the general scalar transport equation into algebraic equation which can be solved numerically. The transport equation is integrated about each control volume, which results in discrete equation, and can be expressed as the conservation law on a control-volume. For an arbitrary control volume$V$, the unsteady conservation equation for the scalar transport quantity $\emptyset$ can be expressed as

$$\int_V \frac{\partial \rho \phi}{\partial t} dV + \oint \rho \phi \, \vec{v} \cdot \, d\vec{A} = \oint \Gamma_\phi \nabla \phi \, d\vec{A} + \int_V \, S_\phi \, dV \qquad 4.64$$

where ρ is the density, $\vec{v}$ is velocity vector, $\vec{A}$ is surface area vector, Γ_ϕ diffusion coefficient of $\nabla \phi$ is the gradient of ϕ and S_ϕ is the source of ϕ per unit volume. Equation 4.64, when applied to each cell in the computational domain as shown in Fig. 4.12, results in discrete algebraic equation 4.65.

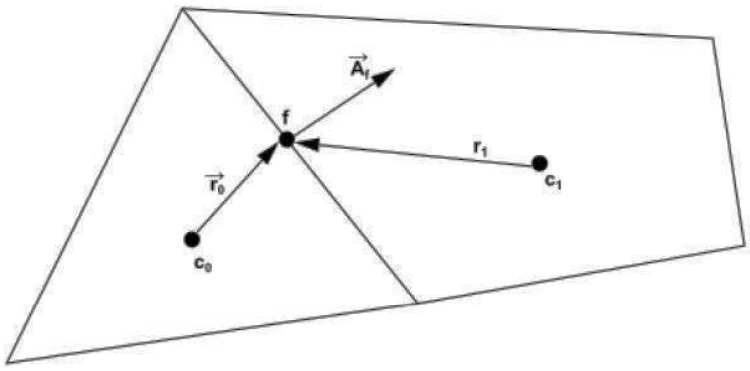

Fig. 4.11: Discretization of a Transport Equation over a Finite Control Volume

$$\frac{\partial \rho \phi}{\partial t} V + \sum_{f}^{N_{faces}} \rho_f \vec{v}_f \emptyset_f \cdot \vec{A}_f = \sum_{f}^{N_{faces}} \Gamma_\phi \nabla \emptyset_f \cdot \vec{A}_f + S_\phi V \qquad 4.65$$

where

N_{faces} = number of faces enclosing cell

$\emptyset_f$ = value of $\emptyset$ convected through face f

$\sum_f^{N_{faces}} \rho_f \vec{v}_f \cdot \vec{A}_f \equiv$ mass flux through the face f

$\vec{A}_f$ = area of the face f

$\nabla \emptyset_f$ = the gradient of $\emptyset$ at face f, and

V = cell volume.

Equation 4.65 readily applies to multi-dimensional, unstructured meshes and contains an unknown variable $\emptyset$ at the cell center and also at the neighboring surrounding cells. Therefore, it is in non-linear with respect to these variables and the linearized form of these equations can be written as

$$a_P \phi = \sum_{nb} a_{nb} \phi_{nb} + b \qquad 4.66$$

where a_P and a_{nb} are the linearized coefficient for ϕ and the subscript nb refers to the neighbor cells. Equation 4.66 is written for each cell in the mesh, which yields to a set of algebraic equations. This linear system of equations is solved iteratively using a point implicit solver in conjunction with an Algebraic Multigrid (AMG) method.

4.7.2. Algebraic Multigrid Method

Multigrid methods are used in the CFD simulation to speed up the convergence of the solver by calculating the corrections on a coarse grid levels. This scheme significantly reduces the number of iterations and the processing time required to attain the converged solution. In this method, the low frequency error or the global error which exist on the fine mesh can be represented on a coarser mesh where it again becomes accessible as high frequency or local error, because of the lesser coarse cell, the global correction can lead to more speedily between adjacent cells. Since the computation on a coarser mesh is performed at a lesser expense in both memory storage and CPU time, it leads to the elimination of the global error at a very fast rate. The basic concept of multigrid can be expressed by considering a set of linearized equations given by 4.73.

$$A\emptyset_e + b = 0 \qquad 4.67$$

where $\emptyset_e$ is the exact solution. Before the convergence is achieved, a defect d exists with the approximate solution $\emptyset$, such that

$$A\emptyset + b = d \qquad 4.68$$

For obtaining the exact solution, a correction of ψ should be applied to ϕ which can be given by Equation 4.69.

$$\phi_e = \phi + \psi \tag{4.69}$$

Substituting this in Equation (4.67), yields to Equation (4.70) or (4.71)

$$A(\phi + \psi) + b = 0 \tag{4.70}$$

or

$$A\psi + (A\phi + b) = 0 \tag{4.71}$$

Equation (4.68) and (4.70) can be combined to obtain

$$A\psi + d = 0 \tag{4.72}$$

Equation 4.72 is the equation for the correction in the defect, d solved on the fine mesh. The high frequency errors or local errors are damped by the relaxation scheme; the correction ψ is then smoothened and solved more effectively on the coarser mesh. The multigrid approach has two basic steps viz., restriction and prolongation. Transferring the defect from fine mesh to coarse mesh is referred as restriction, while transferring of correction from coarser mesh back to finer mesh is termed as prolongation.

The coarse level correction ψ^H is expressed as

$$A^H\psi^H + Rd = 0 \tag{4.73}$$

where R is the restriction operator which transfer the finer meshes to defect down the coarse meshes and A^H is the coarse mesh operator. The new fine level solution is then given by Equation 4.74.

$$\phi^{new} = \phi + P\psi^H \tag{4.74}$$

where P is the prolonged operator, which transfer coarser level correction to the finer level.

In the Algebraic Multigrid Method the coarse level equations are solved without the use of any re-discretization or geometry at the coarser levels. Because of this feature, AMG is best fit for unstructured meshes. The benefit of AMG is that no coarse meshes have to be stored or constructed and no flux terms need to be calculated at coarse level. Once the equations are linearized, non-linearity is not sensed by the solver till the fine level operator is updated.

4.7.3. The Coupled AMG Solver

The linear system is obtained from the discretization of the transport equations and can be written as Equation 4.75.

$$a_{ij}x_j = b_i \tag{4.75}$$

For a density based solver that uses coupled algebraic multigrid solver with an implicit discretization of the coupled system the resultant system can be expressed as Equation 4.76.

$$[A]_{ij}\vec{X}_j = \vec{B}_i \tag{4.76}$$

where,

$$A_{ij} = \begin{bmatrix} a_{ij}^{11} & a_{ij}^{12} & .... & a_{ij}^{1N} \\ a_{ij}^{21} & a_{ij}^{22} & .... & a_{ij}^{2N} \\ . & & . & . \\ . & & . & . \\ a_{ij}^{N1} & a_{ij}^{N2} & .... & a_{ij}^{NN} \end{bmatrix};\ \vec{X}_j = \begin{bmatrix} x_j^1 \\ . \\ . \\ . \\ x_j^N \end{bmatrix};\ and\quad \vec{B}_{\mathrm{i}} = \begin{bmatrix} b_i^1 \\ . \\ . \\ . \\ b_i^N \end{bmatrix} \tag{4.76a}$$

In Equations 4.76, $\vec{X}_j$ is the unknown vector and $\vec{B}_i$ is the source vector. The above system of linear equations is solved by the Gauss-Seidel smoother.

4.7.4. The Gauss Seidel Smoother

The Gauss-Seidel method solves the equations one at a time and in sequence. In this the previously computed results are used as soon as they are available. It makes two sweeps of unknown in forward and in backward directions. The current code uses both block and point Gauss-Seidel smoother for solving systems of equations for the AMG method.

Using the scalar Equation (4.75), the Gauss-Seidel technique can be described. The forward sweep is expressed as per Equation 4.77.

$$x_i^{k+1/2} = \left(b_i - \sum_{j<i} a_{ij} x_j^{k+1/2} - \sum_{j>i} a_{ij} x_j^k \right) \Big/ a_{ii} \quad (i = 1, 2, \ldots\ldots N) \qquad 4.77$$

where N is the number of unknowns. The forward sweep is followed by a backward sweep and can be expressed as per Equation 4.78.

$$x_i^{k+1} = \left(b_i - \sum_{j<i} a_{ij} x_j^{k+1/2} - \sum_{j>i} a_{ij} x_j^{k+1} \right) \Big/ a_{ii} \qquad 4.78$$

From Equations 4.77 and 4.78, the Gauss-Seidel method can be written in matrix form as a two stage recursive solution procedure given by Equation 4.79.

$$(D_A + L_A) D_A^{-1} (D_A + U_A)(x^{k+1} - x^k) = b - Ax^k \qquad 4.79$$

where D_A, U_A, L_A and represents diagonal, upper triangular and lower triangular array of matrix respectively.

4.7.5. Spatial Discretization

In the CFD solver used, the values of the primitive ϕ variables are stored at the cell centers that are also the computational nodes. The face value ϕ_f for the convection term expressed in equation (4.65) must be interpolated from the cell

center value. This is usually done using an upwind scheme for a convection dominated problem as the current case is. In this the face value ϕ_f is derived from quantities in the cell "upwind," relative to normal velocity, v_n. In the present research a second-order upwind scheme has been used because flow filed variables are solved using multidimensional linear reconstruction approaches which are best described for unstructured meshes [82].

In the second-order upwind scheme the face value ϕ_f is computed as per Equation (4.80)

$$\phi_{f,SOU} = \phi + \nabla\emptyset + \vec{r} \qquad 4.80$$

where $\nabla\phi$ and ϕ are the gradient and cell-centered value in the upstream cell, and $\vec{r}$ is the displacement vector from upstream cell centroid to the face centroid.

4.7.6. Evaluation of Inviscid Fluxes

Maximizing both accuracy and efficiency are the primary importance of any algorithm in numerical analysis. Since the numerical behaviour of the viscous and inviscid fluxes is entirely different, it is quite common to split the viscous and inviscid fluxes and discretize them separately through established flux vector splitting schemes [83 to 91]. Liou and Van Leer tested three techniques viz. the Steger-Warming (SWS), Van Leer (VLS) and Roe-Splitting (RS) for variety of problems regarding their accuracy and efficiency [88]. Flux vector splitting (FVS) such as VLS and SWS have proved to be a simple and useful technique for arriving at upwind differencing and is preeminently suited for use in implicit schemes. Unfortunately, the simplicity of these two splitting comes at a price of reduced accuracy due to numerical diffusion. Flux difference splitting (FDS) such as Roe-Splitting (RS) and Osher's Splitting (OS), however has shown to be very accurate and particularly well suited for explicit upwind formulations, Nevertheless, the increased accuracy is accomplished with an increased operation

count and complexity in arriving at the complete linearization of flux formulas for the implicit schemes. Hence, the simplicity of FVS is still motivating researchers to investigate new ways of splitting and combination of FVS and FDS that do away with the problem of numerical diffusion with only a small increase in complexity. A new flux splitting scheme viz. the Advection Upstream Splitting Method (AUSM) was proposed by Liou, which is remarkably simple and accurate and yields a vanishing numerical diffusion [88]. Unlike the Roe's splitting, this scheme does not involve differentiation of fluxes-Jacobian matrix and hence it is not subject to the difficulty arising from the differentiation. Specifically the pressure derivatives, with respect to density and internal energy do not explicitly appear in the flux formulas. This scheme has an advantage of both flux vector and flux difference splitting [89].

The AUSM+ Scheme

This scheme is the modified version of the upwind concept introduced by Liou and Steffen. This scheme defines the cell interface Mach number with the neighboring cell based on characteristic speeds. The inviscid fluxes are defined by the upwind extrapolation of interface Mach number. A modified upwind splitting method for pressure splitting function and generalized Mach number is described by Liou [89], [90] & [91] and is termed as AUSM+. In this the flux is split into two separate distinct parts so that they may be suitably upwind stenciled. The flux-function, $\mathbf{F(w)}$, can be written as the sum of convective flux $\boldsymbol{F^c}$ and a pressure flux $\boldsymbol{P}$ as given by Equation 4.81

$$\mathbf{F(w)} = \mathbf{F}^{(c)} + \mathbf{P} \tag{4.81}$$

where

$$\mathbf{F}^{(c)} = Ma\boldsymbol{\Psi}, \qquad \boldsymbol{\Psi} = \begin{bmatrix} \rho \\ \rho u \\ \rho H \end{bmatrix} \quad \text{and} \quad \mathbf{P} = \begin{bmatrix} 0 \\ p \\ 0 \end{bmatrix} \tag{4.82}$$

Here M is the Mach number and a the speed of sound, $M = ua^{-1}$. The advantage of AUSM+ scheme is that Jacobian matrix is not required to be calculated. In this scheme the flux function is expressed as

$$\mathbf{F}^{*}_{i+\frac{1}{2}} = \frac{1}{2} a^{n}_{i+\frac{1}{2}} \left(m^{n}_{i+\frac{1}{2}} (\boldsymbol{\Psi}^{n}_{i+1} + \boldsymbol{\Psi}^{n}_{i}) - \left| m^{n}_{i+\frac{1}{2}} \right| (\boldsymbol{\Psi}^{n}_{i+1} - \boldsymbol{\Psi}^{n}_{i}) \right) + \mathbf{P}^{n}_{i+\frac{1}{2}} \qquad 4.83$$

where $m^{n}_{i+\frac{1}{2}}$ is the interface quantity of Mach number, which is expressed as Equation 4.84

$$m^{n}_{i+\frac{1}{2}} = \mathcal{M}^{+}(M^{n}_{i}) + \mathcal{M}^{-}(M^{n}_{i+1}) \qquad 4.84$$

with

$$\mathcal{M}^{\pm}(M) = \begin{cases} \frac{1}{2}(M \pm |M|) & if\,|M| \geq 1 \\ \pm\frac{1}{2}(M \pm 1)^2 \pm \beta(M^2 - 1)^2 & otherwise \end{cases} \qquad 4.85$$

The numerical approximation of the speed of sound at the cell interface is done using Equation 4.86

$$a^{n}_{i+\frac{1}{2}} = \sqrt{a^{n}_{i} a^{n}_{i+1}} \qquad 4.86$$

The Mach number at the computational nodes is approximated using Equation 4.87.

$$M^{n}_{i} = \frac{u^{n}_{i}}{a^{n}_{i+\frac{1}{2}}} \quad \text{and} \quad M^{n}_{i+1} = \frac{u^{n}_{i+1}}{a^{n}_{i+\frac{1}{2}}} \qquad 4.87$$

and the pressure term at the cell interface is approximated as

$$\mathbf{P}^n_{i+\frac{1}{2}} = p^+(M_i)\mathbf{P}^n_i + p^-(M_{i+1})\mathbf{P}^n_{i+1} \qquad 4.88$$

where

$$p^{\pm}(M) = \begin{cases} \frac{1}{2}(1 \pm sign\,(M)) & \text{if } |M| \geq 1, \\ \frac{1}{4}(M \pm 1)^2(2 \mp M)\alpha M(M^2-1)^2 & \text{otherwise} \end{cases} \qquad 4.89$$

The value of α and β used in Equations 4.85 and 4.89, as suggested by Liou [91] are

$$\alpha = \frac{3}{16} \quad \text{and} \quad \beta = \frac{1}{8}$$

The AUSM+ scheme has shown a numerous desirable properties as it gives the exact resolution of the shock discontinuity, and is free of oscillations at moving and stationary shocks.

4.7.7. Temporal Discretization

For the transient cases the governing equation is discretize both in time and space. Although the current research presents the steady state results, it is a general practice to obtain the steady state solution using time marching approach wherein unsteady equations are solved. The temporal discretization includes the integration of time derivative term in the differential equations over the time step Δt.

The time derivative of a transport of a variable $\emptyset$ is expressed as

$$\frac{\partial \emptyset}{\partial t} = F\,(\emptyset) \qquad 4.90$$

where the F represents an appropriate function for any spatial discretization. If the first order temporal discretization is done using forward difference, then the temporal discretization is expressed as

$$\frac{\emptyset^{n+1} - \emptyset^{n}}{\Delta t} = F(\emptyset) \qquad 4.91$$

Since the explicit time stepping is subject to stability constraints, an implicit time stepping is often used for steady state solutions as time accuracy is not that important. In Implicit time integration, the time derivative is discretized as per Equation 4.92 with $F(\emptyset)$ evaluated at the future time level.

$$\frac{\emptyset^{n+1} - \emptyset^{n}}{\Delta t} = F(\emptyset^{n+1}) \qquad 4.92$$

The above equation is solved iteratively at each time step before moving it into next step. The advantages of implicit scheme are that it is unconditional stable with respect to time step size.

4.7.8. Gradients Evaluations

To compute the secondary velocity derivatives and diffusion terms, gradients are required. The convection and diffusion terms are discretized using the gradient $\nabla\emptyset$ for a given variable $\emptyset$ in the flow conservation equation. In the present research the Least Square Cell-Based gradient method has been used, in which the solution is assumed to vary linearly. The change in the cell value between the centroids of cell $c0$ and ci along the direction vector $\boldsymbol{r}_i$, as shown in Fig. 4.13, can be expressed as

$$(\nabla\phi)_{c0} \cdot \Delta r_i = (\phi_{ci} - \phi_{c0}) \qquad 4.91$$

where $\nabla\phi$ is the cell gradient. Similar equations are written for each cell surrounding the cell c_0, in order to obtain a system of equations given by Equation 4.92

$$[\,J\,](\nabla\emptyset)_{c0} = \Delta\emptyset \qquad 4.92$$

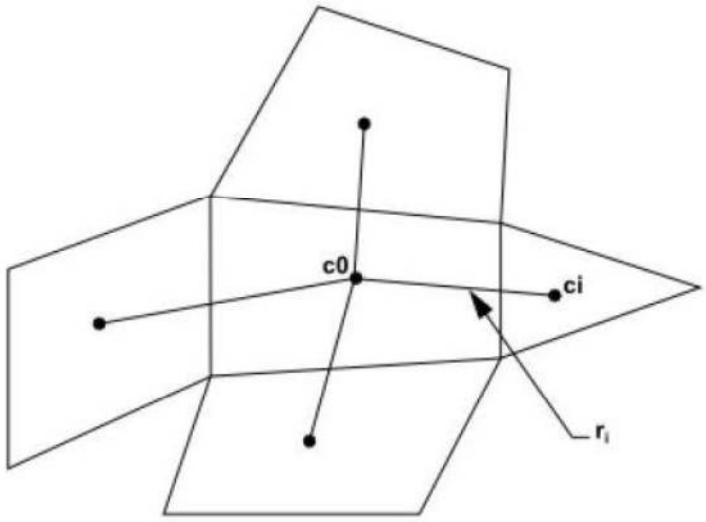

Fig. 4.12: Evaluation of Gradient at Cell Centroid

where [J] is the coefficient matrix that is purely a function of geometry. The above system is solved through minimization problem of non-square coefficient matrix in a least square sense. This system of linear equation is solved by using Gram-Schmidt process [92] i.e. by decomposing the coefficient matrix. This Scheme is used for computing implicit upwind algorithm mainly for unstructured meshes. The above equation yields a matrix of weight in each cell. Thus for the cell centered scheme three component of weights are produced for each faces of cell $c0$.

Therefore gradient at cell centered is expressed as the weight fraction multiply by the difference vector given by Equation 4.93.

$$\nabla\phi = (\phi_{c1} - \phi_{c0}) \qquad 4.93$$

The components of the gradient vector are thus given by Equations 4.94-4.96.

$$(\phi_x)_{c0} = \sum_{i=1}^{n} W^x\, i0 \cdot (\phi_{ci} - \phi_{c0}) \quad 4.94$$

$$(\phi_y)_{c0} = \sum_{i=1}^{n} W^y\, i0 \cdot (\phi_{ci} - \phi_{c0}) \quad 4.95$$

$$(\phi_z)_{c0} = \sum_{i=1}^{n} W^z\, i0 \cdot (\phi_{ci} - \phi_{c0}) \quad 4.96$$

The accuracy of a least square gradient method on skewed and distorted i.e. unstructured meshes is comparable to node based gradient. Also for computation the least square gradient is less expensive than node based gradient method.

4.8. Boundary Conditions

The most crucial aspect numerical simulation is the designation of its boundary conditions which directs the solution toward correct values in an iterative procedure. In the present research flow around 2-dimansional axisymmetric geometric configurations at zero angle of attack has been investigated. Owing a small domain of dependence for hypersonic flows, the upstream boundary is kept at 0.5D ahead of the stagnation point while the radial boundaries are present as 2.5D to capture the shock waves properly. The downstream boundary is a characteristic based supersonic outflow boundary and hence not extended beyond the body as can be seen in Fig. 4.14. As shown in Fig. 4.14, the inlet and the outlet boundaries are designated as pressure farfield wherein the freestream Mach number and static conditions at a distance from the body are specified.

At the outflow boundary also a pressure farfield type boundary has been designated. However no variable specification is required as this being a supersonic outflow, all variables are extrapolated from the interior of the domain. The surface of the models are defined to be isothermal wall at a temperature of T_w =300K for all investigated geometries. This specification leads to the computation

of surface heat fluxes as a part of the solution. Also a no slip wall conditions, i.e. $u_w = v_w = 0$, was applied to the viscous surface of the models. In order to simulate the three dimensional effects at zero degrees angle of attack the line of symmetry has be assigned an axis type boundary condition across which the flowfield gradients are zero. This selection makes the numerical simulation slightly quicker because no extrapolation is necessary.

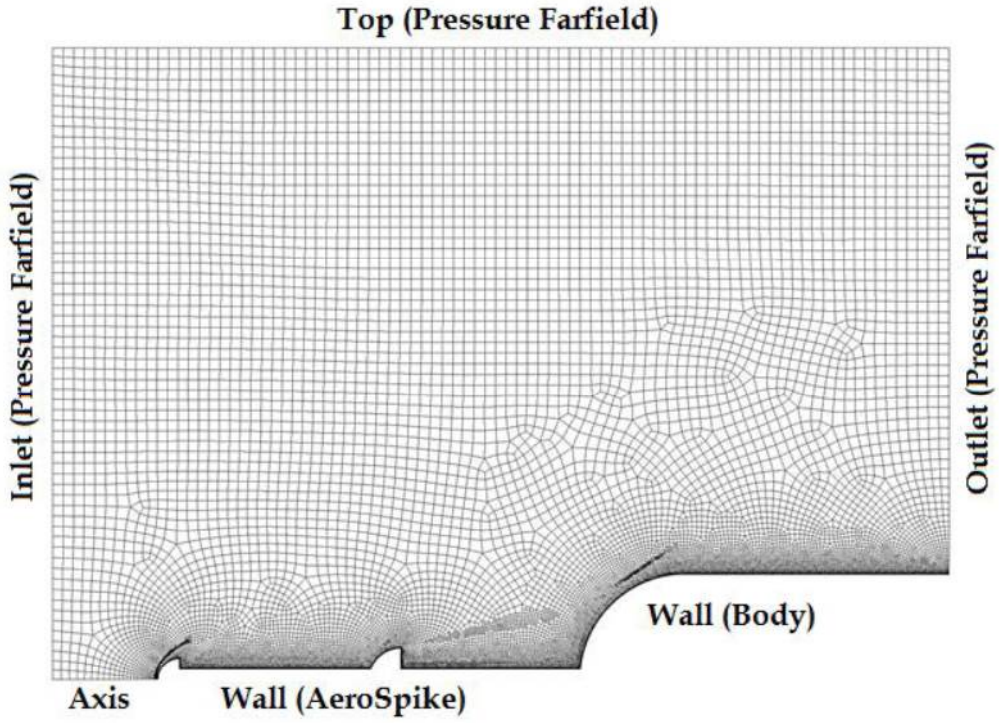

Fig. 4.13: Numerical Boundaries around a Spiked Configuration

A faster convergence can be achieved, and thus a shorter computation time, when the initial conditions are chosen as close as possible to the final steady state values. For high speed flow the definition of freestream values as the initial guess provides very good first approximation of the solution. Hence the freestream values at the pressure farfield boundaries as given in Table 4.1 are also used as the initial conditions in all the cells. Based on the freestream values and the base diameter the Reynold number for present computation is 2.64×10^7, which is high enough to consider the recirculating flows to be fully turbulent, so the effect

of turbulent flow also taken into account by considering suitable turbulence model [73] [74] & [76]. The freestream turbulence level based on extensive literature is specified with a value of turbulent viscosity ratio to be 2.

Table 4.1: Freestream and Initial Conditions

	Symbol	**Units**	**Values**
Mach number	M	-	6.2
Temperature	T	K	216.65
Pressure	P	N/m^2	16066
Molecular viscosity	μ	$Kg/m\text{-}s$	1.785×10^{-5}
Unit Reynolds number	Re	m^{-1}	$2.64X10^7$

4.9. Mesh Independency Study

A grid independence study has been carried out for an arbitrarily selected hemispherical three disk aerospike. The surface pressure distribution for various mesh refinement levels for the above geometry is shown in Fig. 4.15. As can be seen in Fig. 4.15, only the peak reattachment pressure seems to vary as the grid is refined from the starting mesh which has approximately 48,000 cells. But as the number of cells is increased beyond 83511 up to 143765 cells, the surface pressure at all locations almost remains the same. That means the surface pressure and thus the drag and aerodynamic heating for the meshes with 83511, 112980, 126384 and 143765 are almost same. Hence the solution can be assumed to be grid independent for cell count of 83,511 and beyond. Nevertheless, all computations have done with a minimum cell count of 150,000 and going up to 200,000 after adaptive refinement.

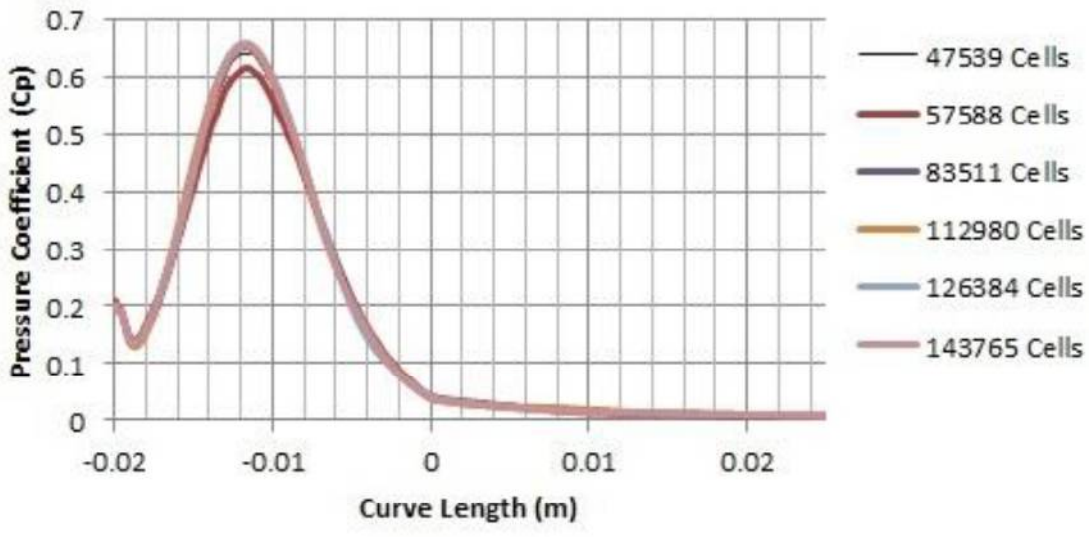

Fig. 4.14: Surface pressure distribution for various grid refinements

4.10. Solver Validation

Computational Fluid Dynamics is a complementary approach to study fluid dynamics and should be supported by either experimental or analytical evaluations. The methodology and the techniques used in must be validated against benchmark experimental value. A solver validation study has been conducted for a sharped edged hemispherical spike against the experimental data available in open literature [19]. The geometrical model considered for the validation experimental data is a 29.718 *mm* diameter hemisphere-cylinder with a sharp tip aerospike of *l/D* ratio equal to 1 for a freestream Reynolds number of 1.2 x 10^6 and Mach number of 6.8. The computed normalized heat fluxes obtained by the solution of axisymmetric Navier Stokes equations show a strong agreement with the experimental values as can be seen in Fig. 4.16. As can be seen in Fig. 4.16, the normalized heat fluxes at different radial locations on the surface differ from the experimental values by less than 10%. Apart from the surface heat flux distribution the drag values for hemispherical blunt body with and without aerodisks for an *l/D* of 1 is also compared to the available experimental values.

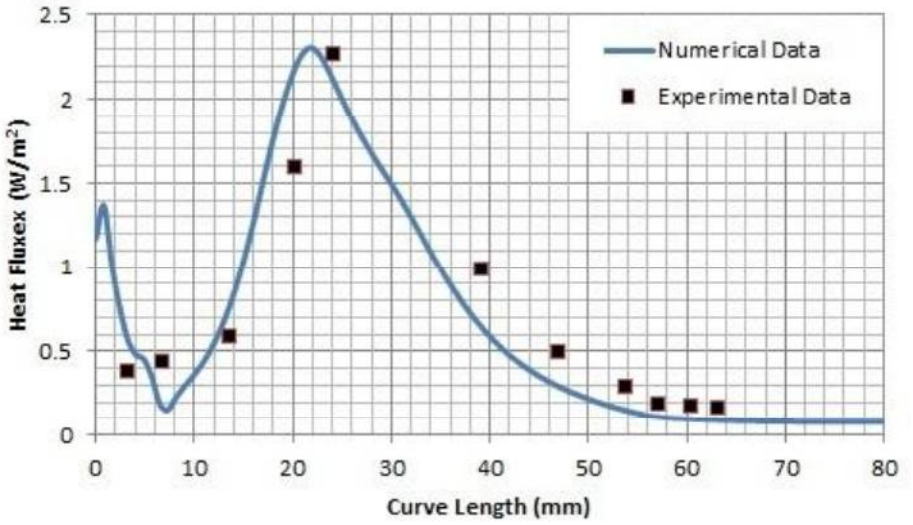

Fig.4.15: Heat flux distributions for spiked hemisphere cylinder [19]

Table 4.2 compares the drag coefficient obtained with the currents numerical setup with the experimental results available in literature [53, 54]. A small amount of difference in the values of drag coefficient seen is probably because of the fact that the simulations are done with fully turbulent assumptions while the experiments done in laminar environment.

Table 4.2: Comparisons of Drag coefficients [53, 54]

	Blunt body	Hemispherical aerodisk l/D=1	Hemispherical aerodisk l/D=1.5	Hemispherical aerodisk l/D=2.0
Experimental	0.90	0.38	0.275	0.225
Numerical	0.91	0.37	0.320	0.280

Thus it can be assumed that the current solver FLUENT provide reasonably accurate results for the techniques adopted in the research. These results are also in consistent with the results obtained by Yadav and Guven [64]. This suggests that the Numerical methodology adopted in the current research is an acceptable one for meaningful insights into the flow analysis of complex hypersonic flows.